

Local structures and damage processes of electron irradiated α -SiC studied with transmission electron microscopy and electron energy-loss spectroscopy

Shunsuke Muto^{a)} and Tetsuo Tanabe

Center for Integrated Research in Science and Engineering, Nagoya University, Chikusa-ku, Nagoya 464-8603, Japan

(Received 8 October 2002; accepted 3 January 2003)

Damaged structures of α -SiC below and above the critical temperature of amorphization (T_c) under high-energy electron irradiation were studied by means of transmission electron microscopy and electron energy-loss spectroscopy. Above T_c , crystal fragmentation takes place due to local lattice strains caused by preferential displacements, subsequent outward diffusion of carbon atoms and formation of silicon nano-clusters. On the other hand, the amorphous structure formed below T_c can be well characterized by the formation of Si-Si, Si-C, and sp^3 C-C covalent bonds with the tetrahedral coordination locally retained and uniformly distributed. The primary amorphization process under electron irradiation can be interpreted by the defect-accumulation model, in which displaced atoms are frozen at interstitial sites before long-distance diffusion by reconstructing the surrounding structure to relax the local strains. Accordingly the amorphization process is controlled essentially by the mobility of displaced carbon and silicon atoms, and chemical disordering seems to play a minor role in triggering the amorphization. A key issue for irradiation induced volume swelling of amorphous SiC is also presented. © 2003 American Institute of Physics.

[DOI: 10.1063/1.1555673]

I. INTRODUCTION

Silicon carbide is an attractive material for applications ranging from small electronic devices to larger scale components in nuclear systems. For practical use intensive investigation of the effects of displacive radiation on the structure is required: for the processing of SiC devices, microstructure change by implantation of dopant ions is of importance,^{1,2} while in nuclear applications the significant swelling and changes in mechanical properties during or after high-energy particle irradiation are key issues.³

Numerous studies have reported that SiC is easily amorphized by high-energy particle bombardment (electron,⁴⁻⁶ neutron,^{7,8} and ions⁹⁻¹⁵) below room temperature for damage levels of approximately 0.1–0.5 displacements per atom (dpa). This critical dose for amorphization is rather low, compared to other Si-based ceramics. The crystalline-amorphous transition in SiC has been thus attracted much attention not only from the practical point of view, but also from the fundamental interest in the susceptibility to irradiation-induced loss of long-range order (amorphization) of crystalline solids: in general amorphized structures are not random and are still constrained by topological construction rules, derived from the ways structural elements can be connected together.¹⁶ This concept of *connectivity* was further extended to the degree of structural freedom to classify the susceptibility to irradiation-induced amorphization:¹⁷ the larger the degree of freedom is, the more the structure is under constrained and accordingly is harder to be amorphized.

The idea of the degree of freedom seems to well correlate with the susceptibility to irradiation-induced amorphization for a wide range of ceramic structure types, though a representative exception is SiC among other covalent- or ionic-bonded ceramics having tetrahedral local coordination, such as Si, SiO₂, Si₃N₄, and others. Hobbs *et al.*¹⁶ gave two possible explanations for this apparent discrepancy in SiC: (1) the structure is especially vulnerable to displacement of a vertex atom in a tetrahedron, tetrahedral polytopes being destroyed in a single displacement event; and (2) the possibility of antisite disorder in displacement cascades removes the distinguishability of Si and C.

Bolse¹⁸ has conducted ion irradiation and found that amorphization occurs by nucleation and growth of defect agglomerates in the still crystalline matrix, until a critical damage density is achieved. The local atomic configuration probed by Si K extended x-ray absorption fine structure (EXAFS) has shown that a correlation between neighboring tetrahedral structural units remains even though a highly disordered network of SiC₄-tetrahedra forms. This result excludes possibility (1) above.

Possibility (2) has attracted attention because the stable covalent bonding lengths of Si-C (0.189 nm), Si-Si (0.235 nm), and C-C [0.154 (sp^3) and 0.142 (sp^2) nm] are significantly different from one another, and an antisite defect can act as a strong strain center. However, Grigull *et al.*,¹⁹ from their x-ray diffraction measurements on the 002 superlattice and the 004 fundamental reflections of β -SiC during ion irradiation in a dose range up to complete amorphization, have claimed that the crystalline-to-amorphous (C-A) transition is a continuous process rather than a sudden collapse of a defective crystal structure and that the crystalline state re-

^{a)} Author to whom correspondence should be addressed; electronic mail: muto@cirse.nagoya-u.ac.jp

mains stable locally with respect to amorphization up to a high degree of chemical disorder. Hence possibility (2) is also doubtful as a direct explanation for the small susceptibility to C–A transition of SiC.

Heavy ion or fast neutron irradiation brings about cascade damage, in which extreme structural mixing at very localized regions occurs. The C–A transition under such conditions may be considered as structural relaxation after local melting around the primary knock-on atoms (PKAs). Actually observation of a neutron-irradiated sample by transmission electron microscopy (TEM) showed a heterogeneous admixture of crystalline and amorphized regions, suggesting that the C–A transition proceeds via density increment of damaged areas. This, however, gives little clear insight for the disordering mechanism itself, because the primary processes occurring within the cascade damage have been still in a black box.

Recent progress in computer simulation techniques has opened a possibility for directly probing the atomistic processes at the very initial stage of irradiation by energetic particle bombardment. Molecular dynamics (MD) simulations based on semiempirical interatomic potentials are now at hand for treating the extremely large number of atoms. Gao and Weber^{20–22} examined by MD the primary damage states produced by tens of keV atom recoils in crystalline SiC. They claimed that the driving force for amorphization is due to local accumulation of Frenkel pairs and antisite defects. A notable finding in their MD simulations is that defect clusters (cascade damage) are created by a quenched-in mechanism directly from the collisional phase of the cascade to their final arrangements, unlike the cases for metals. Perlado *et al.*²³ have also performed MD simulations of neutron damage in β -SiC. They described a situation of damage accumulation by “ductile” Si sublattice and “fragile” C sublattice to express an outstanding capability of recombination of Si recoils and many more defects were produced on the C sublattice than on the Si sublattice. These simulations treated the defects configurations after the cascade damage occurs.

In contrast to the heavy ion or neutron irradiation, high-energy electron irradiation will be more suitable to reveal the primary mechanism of amorphization by sequential accumulation of displacive point defects, because the energy transferred to PKA produces at most several atomic displacements. Inui and Mori^{4,5} intensively studied the C–A transition of SiC by electron irradiation. They used an ultrahigh-voltage TEM (UHV-TEM), and identified the critical temperature (T_c), critical electron energy, and crystal orientation dependence of the incident electron beam for the C–A transition. They also showed that the chemical disordering always preceded the topological disordering. Nevertheless, it is still unclear whether the chemical disordering triggers the topological disordering, and microscopically localized atomic configurations around the displaced atoms should be examined for this purpose. In case of covalent bonded materials, free interstitial atoms should not be stably present without reconstructing the unsaturated bonds with the surrounding atoms.

In the present article the short-range structural correlation in electron-irradiated α -SiC (6H) is examined in detail,

using electron energy-loss spectroscopy (EELS) and TEM. The former technique is especially suitable for probing both spatial and electronic structures of localized regions around a specific atomic element. The outline of this article is as follows: after describing the experimental detail in Sec. II, results of microanalysis of areas electron irradiated above and below T_c are presented in Sec. III. In Sec. IV the microscopic mechanisms of damage processes above and below T_c are discussed, based on the results obtained in Sec. III, and finally the origin of the large volume swelling in SiC by irradiation is also discussed.

II. EXPERIMENT

The sample used here was a commercial (0001) oriented 6H–SiC wafer (n type, Cree Systems, Inc.). It was cut into disks, 3 mm in diameter, followed by mechanical grinding and then Ar ion milling for TEM observation. Electron irradiation was done in an UHV-TEM, Hitachi H-1250ST of Nagoya University above room temperature (RT). The critical temperature T_c for amorphization was reported to be slightly below RT.⁴ The irradiation was done with a focused electron beam (~ 400 nm in diameter) at an accelerating voltage of 1.0 MV with a dose rate of 1.8×10^{25} e/m² s. Electron irradiation at a low temperature was done in a UHV-TEM, JEOL ARM-1300 of Hokkaido University at an accelerating voltage of 1.25 MV at 108 K with a dose rate of 1.2×10^{24} e/m² s. The diameter of the focused beam was about 800 nm. The electron dose is hereafter expressed in dpa, which is the number of Frenkel pairs formed per incident ion. In the present study the dpa rate was calculated by $\phi\sigma_d$, where ϕ is the experimental electron flux and σ_d is the cross section for the displacement damage by electrons. σ_d for electrons having the energy E greater than E_d was calculated with the McKinley–Feshbach formula²⁴

$$\sigma_d(E) = \frac{\pi}{4} b^2 \left[\left(\frac{T_m}{E_d} - 1 \right) - \beta^2 \ln \frac{T_m}{E_d} + \pi\alpha\beta \left\{ 2 \left[\left(\frac{T_m}{E_d} \right)^{1/2} - 1 \right] - \ln \frac{T_m}{E_d} \right\} \right], \quad (1)$$

where $(\pi/4)b^2 = \pi Z_2 r_0^2 (1 - \beta^2) / \beta^4$; $\beta = v/c$ that is the ratio of electron and light velocities, Z_2 is the atomic number of the target atom, and r_0 is the Bohr radius; $\alpha \cong Z_2/137$; E_d is the threshold energy where an atom is always displaced from its lattice site when it receives energy greater than E_d and is never displaced at lower energy, and T_m is the maximum energy which can be transferred in a collision by an electron of kinetic energy E

$$T_m = \frac{2(E + 2mc^2)}{M_2 c^2} E, \quad (2)$$

where M_2 is the target atomic mass. An MD calculation gave $E_d = 40$ –110 eV for Si and 25–60 eV for C, depending on the displaced directions.²³ We estimated the average cross section for SiC by taking $E_d = 70$ and 40 eV, respectively, for Si and C. The dpa values of SiC is derived simply by taking the average cross sections for the displacement damage of Si and C.

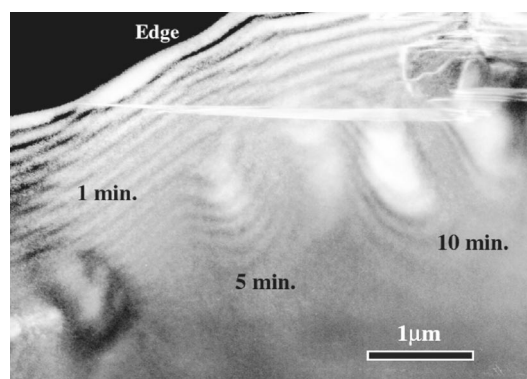


FIG. 1. Dark-field image of electron irradiated 6H-SiC, showing strain contrasts around the areas irradiated at RT for 1, 5, and 10 min.

The irradiated samples were subsequently examined in a JEOL JEM200CX TEM equipped with a GATAN model 766 EELS, operated at 160 kV. A part of EELS spectra were obtained with a Phillips CM-300 equipped with GATAN imaging filter, at EMAT, University of Antwerp, operated at 300 kV. A JEOL JEM3000F TEM equipped with GIF at The Wakasawan Energy Research Center was also used for energy-filtered imaging of the irradiated areas.

III. RESULTS

A. Local structure of areas irradiated above T_c

1. TEM observation and electron diffraction

The irradiated area started to exhibit a strong strain contrast immediately at the onset of the irradiation at RT. The strain contrast gradually developed by the prolonged irradiation. A dark-field image in which three spots correspond to areas irradiated for 1, 5, and 10 min (0.09, 0.45, and 0.9 dpa, respectively) from the left to the right, respectively, is shown in Fig. 1. The irradiated areas exhibit so-called coffee-bean strain contrasts typical for isotropic dilation or contraction.²⁵

A weak-beam dark-field image after 1.8 dpa irradiation and a zone-axis electron diffraction pattern taken from the irradiated area are shown in Fig. 2(a). Fine defect contrasts are seen over the whole irradiated area, although the associated diffraction pattern exhibited no indication of lattice defects, such as extra diffraction spots, halo rings, or any distortion of the original diffraction spots. Instead, the background intensities around the low-order diffraction spots were apparently increased by the irradiation. This indicates that the crystal structure was generally well retained, though it contained a high density of defects less than about 1 nm in size over the irradiated area. Figure 2(b) is an enlarged image of a thicker part in Fig. 2(a). The lattice fringes corresponding to the unit cell dimension in the c axis are slightly bent from place to place, as indicated by arrows in the figure. From the above observations we have attributed the defect contrasts to the local lattice bending resulting from the displacement damage. The lattice bending gives rise to slight misorientation locally. These local elastic strains would not change the diffraction pattern appreciably. The same experiment was repeated on an area thicker than $2 \mu\text{m}$. After the irradiation of 20 min (1.8 dpa), the irradiated area was

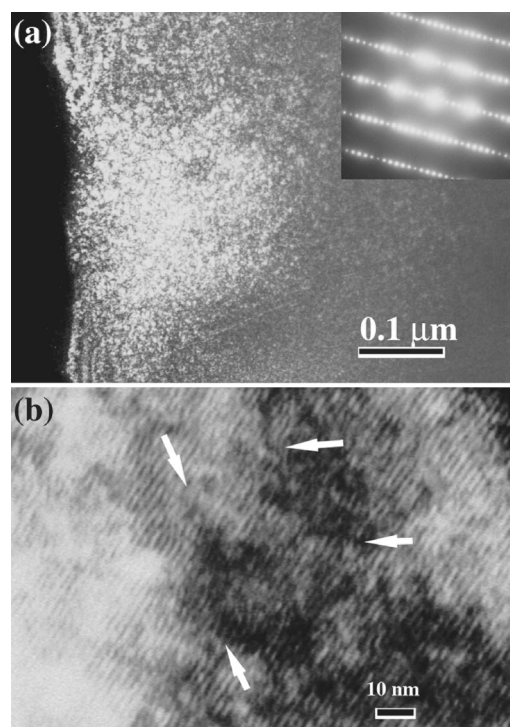


FIG. 2. (a) Weak-beam dark-field image of 6H-SiC irradiated at RT for 30 min (2.4 dpa), and associated zone-axis electron diffraction pattern from the same area. (b) Enlarged portion of (a). Note bends of the lattice fringes indicated by arrows.

slightly thinned by ion milling for better TEM observation. As a result similar fine defect contrasts were observed and hence the effect was not a thin foil effect.

A very thin part ($\sim 5\text{--}10 \text{ nm}$) of the irradiated area was observed in a multibeam lattice-imaging mode. Obtained high-resolution images of the area irradiated for 1 and 20 min are shown in Figs. 3(a) and 3(b), respectively, together with the corresponding fast Fourier transform (FFT) power spectra. No distinct difference is observed not only between the two images but also between the two power spectra except a slight increase of diffuse background in (b). This indicates that the displacement damage exerted little influence on the zone-axis image at very thin areas. The lattice bending in the thicker areas [Fig. 2(b)] is likely caused by a dynamical scattering effect, which can enhance the local fluctuation of lattice planes.

2. Plasmon shift

A transmission EEL spectrum from a thin foil material generally exhibits a distinct peak around 10–30 eV, which is interpreted as a bulk plasmon loss. The plasmon energy E_p is expressed by²⁶

$$E_p = \hbar \sqrt{\frac{ne^2}{\epsilon_0 m_0}}, \quad (3)$$

based on the Drude model for metals, where \hbar is the Planck constant, n is the number density of valence electrons, e is the electron charge, m_0 is the electron mass, and ϵ_0 is the dielectric constant of vacuum. Equation (3) predicts 23.1 eV

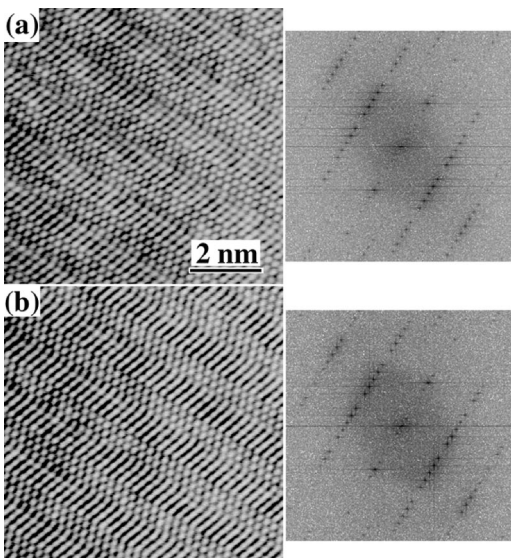


FIG. 3. High-resolution lattice images at a very thin part of the sample after electron illumination for 1 min (a) and 20 min (b). The right column shows the corresponding FFT power spectra of (a) and (b).

for β -SiC, and the experimental plasmon peak was located at 22.5–22.9 eV, in fair agreement with the predicted value.

The plasmon peak energy at the irradiated areas shifted to the lower energy side with increasing electron dose. This redshift depended on the sample thickness of the irradiated areas. The changes in plasmon peak position for thin and thick areas are shown in Fig. 4 as a function of the electron dose. It is seen that the thinner area demonstrated larger plasmon shift. In the present case, the plasmon shift is considered to reflect the change in n , which should correspond to the change in the atomic density because the overall crystal structure and accordingly its electronic structure substantially remained unchanged, as observed in TEM. The decrease in the plasmon energy thus corresponds to the decrease in the atomic density, presumably due to the outward diffusion of displaced atoms. This explains the thickness dependence of the plasmon shift because displaced atoms reach the surfaces and the prolonged illumination by the strong electron flux evaporates the surface layer more effectively in

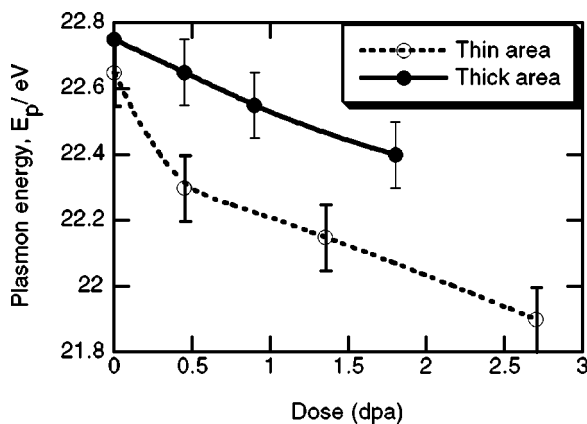


FIG. 4. Changes in plasmon energy as a function of electron dose, taken from a thin (~ 100 nm) and thick (~ 2 μm) area.

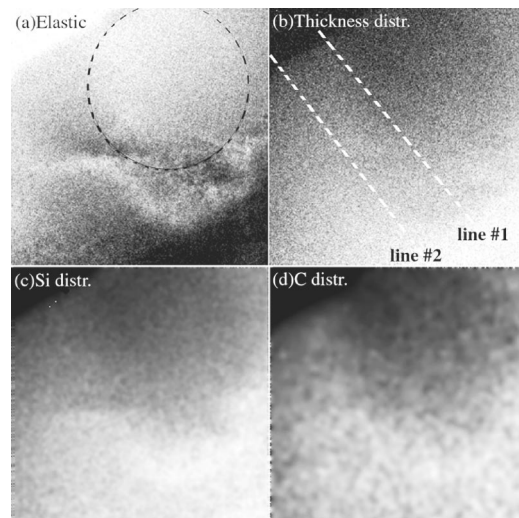


FIG. 5. Energy-filtered images of an area irradiated at RT for 20 min, showing a zero-loss image (a), thickness distribution image (b), and Si (c) and C (d) elemental distribution images, respectively. The electron-illuminated area is shown with the broken circle in (a).

thinner areas. It is known that graphite layers tend to be evaporated by the illumination of an intense electron beam.²⁷ Therefore it can be assumed that lighter carbon atoms were preferentially displaced and diffused away to the surface, followed by the electron-stimulated evaporation.

3. Energy-filtered images

In order to confirm the claim in the previous section, attempts were made to obtain two-dimensional spatial distribution of constituent elements and thickness of the electron-irradiated area, using the energy-filtering TEM. Figures 5(a) and 5(b) show, respectively, an energy-filtered image taken with the elastically scattered electrons only (zero-loss image) and a thickness distribution image. The latter was displayed by computing pixel by pixel the natural logarithm of the intensity ratio of unfiltered and zero-loss image intensities, according to the following general formula²⁸

$$I_0/I = \exp(-t/\lambda). \quad (4)$$

Hence the intensity distribution stands for that of t/λ , where t is the true sample thickness and λ is the mean free path of electron for inelastic scattering. It is seen from the intensity distribution (b) that the irradiated area was slightly thinned compared to the surrounding unirradiated area. This apparent thickness change revealed here can be ascribed to: (i) a real thickness variation due to a true mass loss and/or (ii) a change of the mean free path λ at the irradiated area. (ii) can be caused by a change in atomic density, inversely proportional to λ .²⁶ The present apparent reduction of thickness should accompany a net mass loss, because the upper limit of the change in λ was estimated from the plasmon shift to be only $\sim 2\%$.

Figures 5(c) and 5(d) show C and Si distributions, respectively, imaged with C K and Si $L_{2,3}$ core loss spectra, using the three-energy window method for the background subtraction.^{26,29} The intensity profile of (b)–(d) along the broken lines indicated in (b), one across the irradiated area

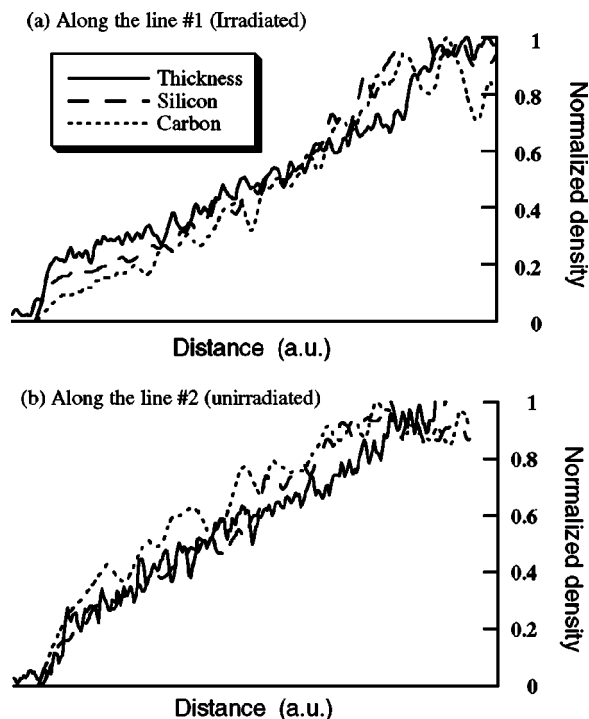


FIG. 6. Intensity profiles of Figs. 5(b)–5(d) along the broken lines No. 1 (a) and No. 2 (b) indicated in Fig. 5(b).

(line No. 1) and the other running outside of the irradiated area (line No. 2), are shown in Figs. 6(a) and 6(b). The intensity profiles were normalized by the background intensity of a thick area far from the irradiated area. Apparently the intensity profiles across the irradiated area exhibit concave characters, in contrast to convex shapes of those outside the irradiated area. This is an unambiguous evidence for the reduction of the true thickness and atom contents at the irradiated area.

4. EXELFS analysis

Extended energy-loss fine structure (EXELFS) is defined as the minute oscillating structure overlaying on the smoothly decayed background intensity extended to the high-energy side of a core loss spectrum over hundreds of eV, which is equivalent to EXAFS on the condition that the dipole selection rule holds.²⁶ The EXELFS analysis leads us to an atomic radial distribution around the excited atom, called a partial radial distribution function (PRDF).

In the preliminary work³⁰ we already reported the detailed analysis of EXELFS data for the irradiation above T_c : in the derived PRDF around silicon the formation of direct Si–Si bonding was clearly observed in the area irradiated up to 1.8 dpa. The size of the Si clusters should be no greater than 1 nm, because there were no extra diffraction spots or halo rings associated with such clusters in the electron diffraction. The EELS elemental analysis indicated that the carbon content is reduced by nearly 10% at the irradiated area.³⁰

Here we have applied the reverse Monte Carlo (RMC) method to the same EXELFS data, to visualize the nanoclustering. This method leads to a three-dimensional atomic configuration by randomly moving atomic positions until the

best fit between the experimental data and calculated one from the resultant atomic positions is obtained, starting with an appropriate initial condition and constraint conditions within the RMC cell containing many atoms, at least more than 1000.^{31–33} EXELFS spectra are particularly sensitive to the short-range order within about 0.4–0.5 nm from the excited atom.³³

In principle the RMC modeling is effective for obtaining a statistically plausible structure for a disordered system. In the present study we are trying to obtain a structure slightly deviated from the well-defined crystalline state, consistent with the experimental spectra. We first tried the RMC fitting of the data from an unirradiated area and confirmed that the experimental EXELFS interference functions were consistent with the crystal structure.³³

For simplicity we started with the β -SiC (cubic) structure instead of 6H, because the difference between the two structures exists in the third nearest neighbor or farther atomic pairs. The RMC cell contained 4096 atoms (2048 carbon atoms and 2048 silicon atoms), which correspond to $8 \times 8 \times 8$ unit cells in size. For the modeling of the irradiated area, the number of carbon atoms was reduced according to the experimentally obtained value. The theoretical interference function $\chi_C(k)$ for each atomic configuration was calculated with the formula

$$\chi_C(k) = \int_0^\infty 4\pi r^2 \rho g_2(r) \gamma^{(2)}(r, k) dr, \quad (5)$$

where ρ is the atomic density, $g_2(r)$ is the pair correlation function, both derived from the atomic positions in the cell, and $\gamma^{(2)}(r, k)$ is the EXELFS interference function for the possible atom pairs having the interatomic distance of r , which is calculated with the FEFF8.2 code.³⁴ The experimental interference functions, $\chi_E(k)$, were acquired and extracted from the Si and C K edges. The atomic density of the irradiated area was not precisely determined, and hence a number of RMC fits were conducted by changing the value as a parameter. No significant difference in the resultant atomic configuration was found. The set of constraint conditions imposed and the other practical details are discussed elsewhere.³³ The RMC modeling will give an atomic configuration, statistically consistent with the three dimensional distribution of interatomic distances of the real structure. Since the EXELFS interference functions contain information within 0.4–0.5 nm from the central excited atom, they are sensitive to the local atom clustering but insensitive to the spatial distribution of the clusters, e.g., uniformly distributed or segregated.

The [110] projection of the atomic configuration obtained by RMC fitting for the area irradiated up to 1.8 dpa is shown in Fig. 7, in which silicon and carbon atoms are separately shown, respectively, in (a) and (b). Atomic bonds are depicted for atom pairs having plausible interatomic distances (Si–C: 0.18–0.20 nm, Si–Si: 0.22–0.25 nm, C–C: 0.14–0.16 nm). The C sublattice remains almost unchanged within the range of ~ 0.02 nm from the equilibrium positions, while the Si sublattice is locally distorted with direct Si–Si bonds formed. The three-dimensional spatial distribution of the Si clustering is better visualized in Fig. 7(c),

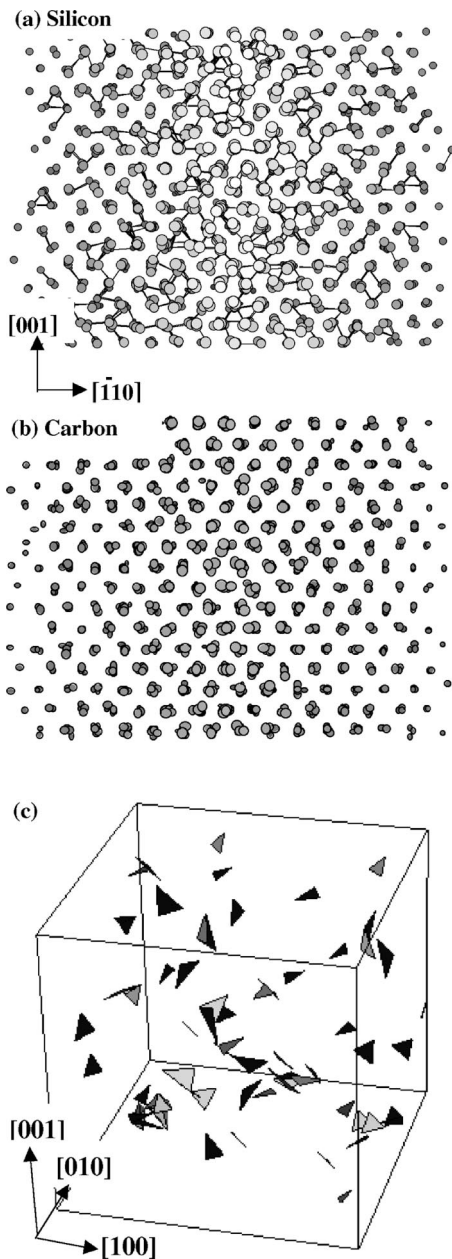


FIG. 7. Projected atomic configurations obtained by RMC fitting of EX-ELFS data in the damaged area: (a) silicon, (b) carbon, and (c) three dimensional display of Si clusters.

generated by the GLASSVIR³⁵ and STRUVIR³⁶ program packages. The figure illustrates Si-Si_n clusters ($n=3-20$) as triangles joining the surrounding Si atoms for $n=3$, and convex polyhedra regarding the Si central atom for $n>3$. The Si clusters consist of no more than four atoms, which would produce almost no effect on the electron diffraction pattern and this is consistent with the experimental result presented in Sec. III A 1.

A lattice image and electron diffraction pattern expected from the atomic positions obtained above can be calculated, based on the dynamical electron diffraction theory.³⁷ The calculated lattice image at the optimum defocus value (Scherzer focus) and diffraction pattern projected onto the (110) plane are shown in Figs. 8(a) and 8(b), respectively. Image (a) shows no appreciable lattice distortion or defective feature,

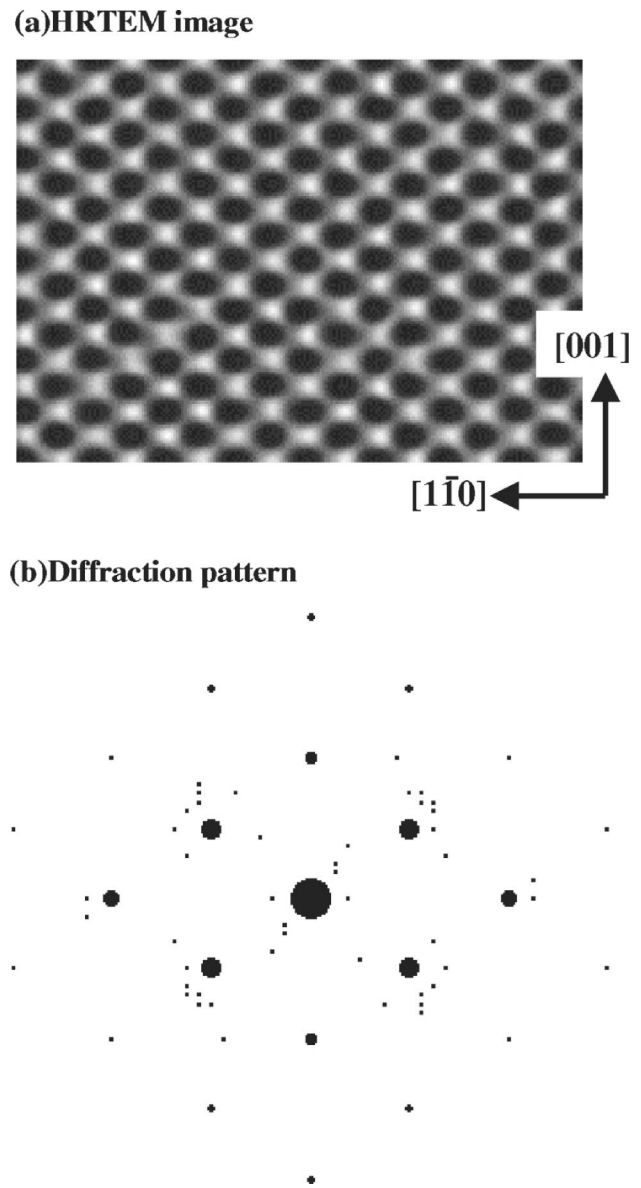


FIG. 8. Calculated high-resolution TEM image (thickness=96 nm, defocus value=50 nm underfocused) (a) and associated electron diffraction pattern, using the atomic positions in Fig. 7.

and the diffraction pattern (b) also exhibits no distinct features reflecting the local atom clustering except slight increase in the background intensity around the diffraction spots. These features qualitatively agree with those obtained experimentally, as presented in Sec. III A 1.

5. ELNES of irradiated area

A core-loss spectrum recorded from a solid specimen shows a pronounced fine structure, taking the form of peaks in intensity within ~ 50 eV of the ionization threshold. This fine structure is called energy-loss near-edge structure (ELNES), and most of this structure reflects the influence of atoms surrounding the excited atom (chemical information).^{26,29}

Si *L* and C *K* ELNES acquired from the unirradiated and 1.8 dpa-irradiated areas are shown in Figs. 9(a) and 9(b), together with those obtained from crystalline Si, amorphous

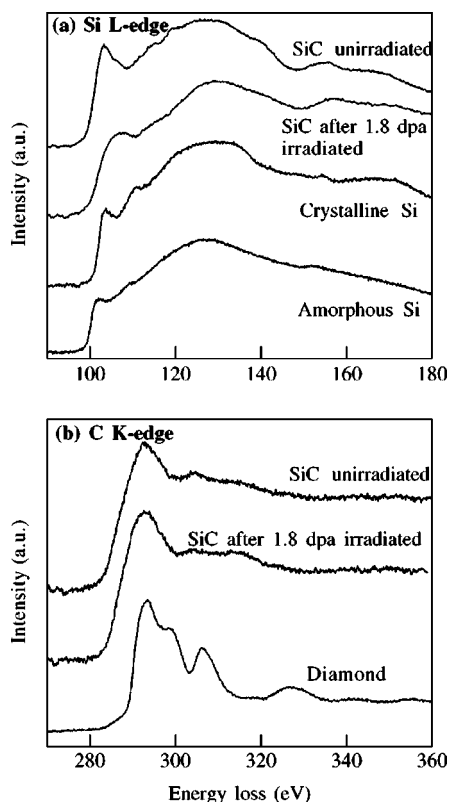


FIG. 9. ELNES of Si *L* edge (a) and C *K* edge (b) from the areas of unirradiated and 1.8 dpa irradiated at RT. ELNES of crystalline silicon, amorphous silicon, and diamond are shown for comparison.

Si (*a*-Si), and diamond for comparison. By the electron irradiation the C *K* ELNES remained almost unchanged, while the first prominent peak of Si *L* edge was broadened and the peak profile around 120–140 eV showed a feature very similar to that of *a*-Si. These indicate that the C–Si₄ tetrahedral configuration was well maintained, whereas the chemical environments around Si significantly changed by the irradiation. The above facts can be consistently explained by the distortions of the Si sublattice, accompanied by the local atom clustering and the rather rigid C sublattice, concluded by the preceding sections.

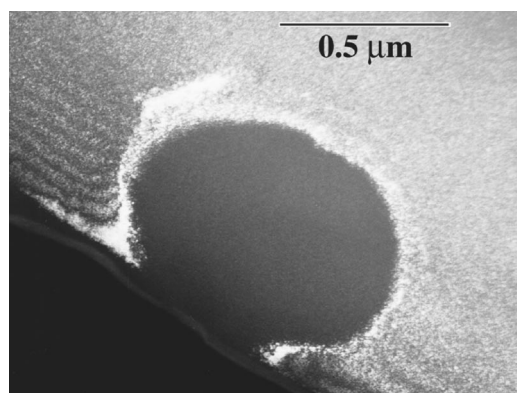


FIG. 10. Dark-field image of 6H-SiC after electron irradiated at 108 K for 40 min. The oval area showing a darker contrast is completely amorphized.

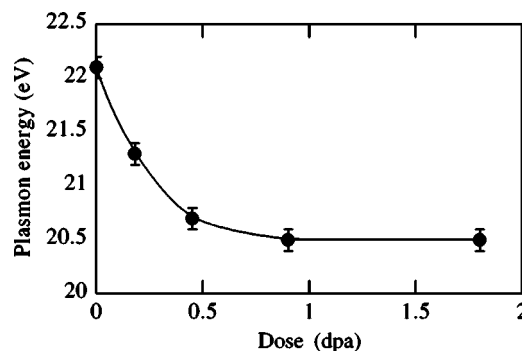


FIG. 11. Change in plasmon energy of the area irradiated at 108 K as a function of electron dose.

B. Amorphous structure formed by irradiation below *T_c*

1. TEM observation and plasmon shift measurement

Figure 10 shows a weak-beam image of SiC electron irradiated by 2 dpa at 108 K. The area of a uniform contrast corresponds to the amorphized area. The plasmon shift with the irradiation at 108 K as a function of electron dose is shown in Fig. 11. It should be mentioned that the plasmon energy at 0 dpa is less than that shown in Fig. 4 by 0.4–0.6 eV; this is presumably due to different energy calibrations of the spectrometer, varying by the external conditions such as temperature and humidity in the laboratory. The plasmon shift well corresponded to the degree of amorphization, monitored by the formation of halo rings in the electron diffraction. The complete halo formation occurred at 0.8–1.0 dpa, well correlated with the saturation of the plasmon shift curve. The final plasmon energy was independent of amorphized temperature and the sample thickness. If assuming the plasmon shift to be due to the reduction of valence electron density, or atomic density of the irradiated area, the corresponding final volume swelling is estimated to be about 14%, which is close to the value observed in neutron irradiation.^{3,8}

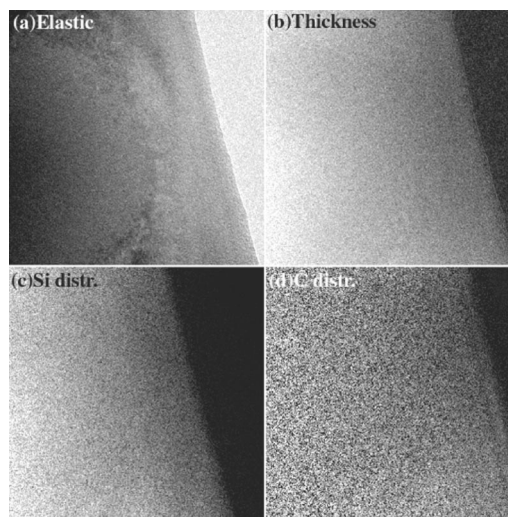


FIG. 12. Energy-filtered images of an amorphized area after irradiation at 108 K for 20 min, showing (a) zero-loss image, (b) thickness distribution, (c) Si, and (d) C elemental distributions.

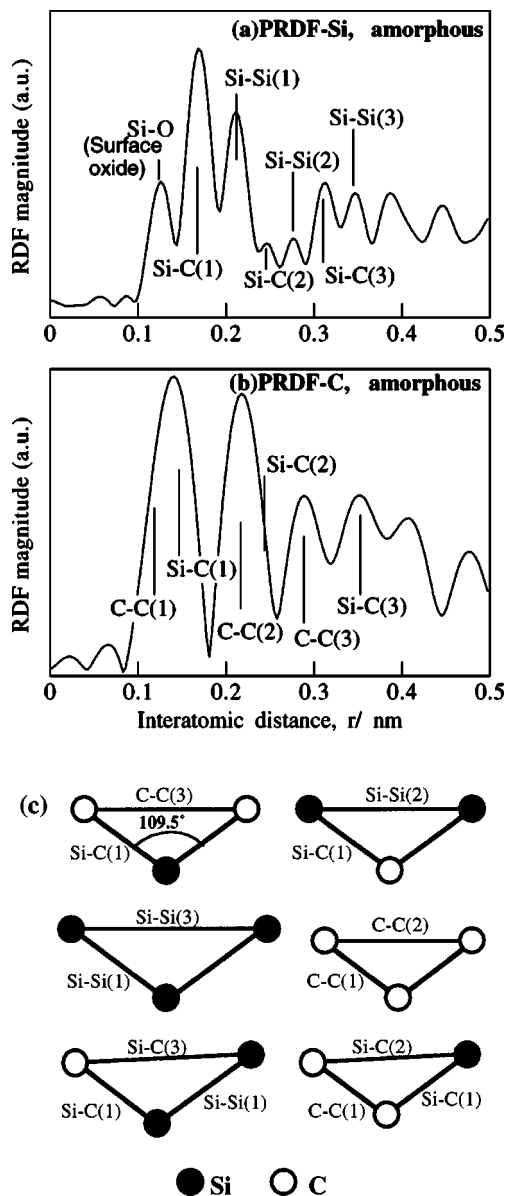


FIG. 13. PRDFs around Si (a) and C (b) in the amorphized area, obtained by EXELFS analysis. (c) Possible atomic configurations of building blocks of the amorphous SiC. Si-Si(1): 0.235 nm, Si-Si(2): 0.309 nm, Si-Si(3): 0.383 nm, Si-C(1): 0.189 nm, Si-C(2): 0.281 nm, Si-C(3): 0.347 nm, C-C(1): 0.154 nm, C-C(2): 0.252 nm, C-C(3): 0.309 nm.

2. Energy-filtered images of amorphized area

The energy-filtering TEM was again applied to examine the thickness and elemental distributions of the amorphized area. A set of obtained images is shown in Figs. 12(a)–12(d). The irradiated (amorphized) area is recognized as an area of a darker contrast in the zero-loss image, (a). In (b)–(d), however, no contrast is observed to distinguish the irradiated area from the unirradiated one. This indicates that the volume swelling, or the increase in the thickness, was completely compensated by the corresponding increment of λ with no net mass loss, and the produced Frenkel pairs during the irradiation did not diffuse away out of the irradiated area, unlike the case for the RT irradiation.

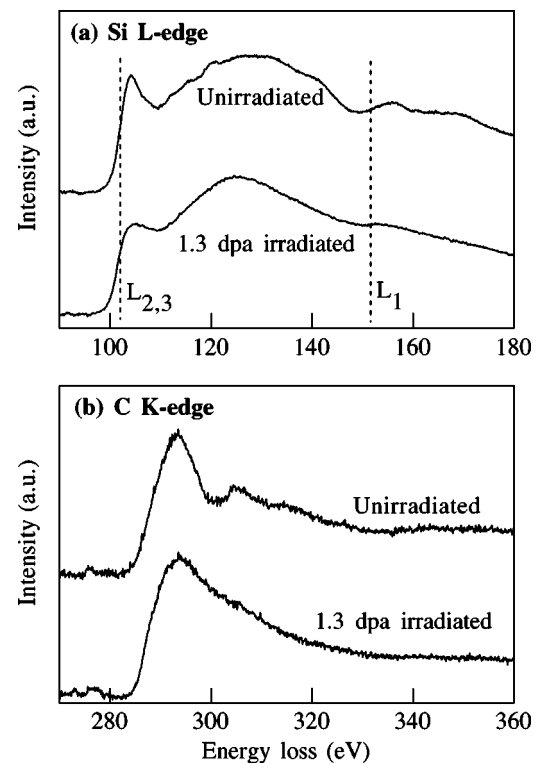


FIG. 14. ELNES of Si *L* edge (a) and C *K* edge (b) from the areas of unirradiated and 1.3 dpa irradiated (amorphized) at 108 K.

3. EXELFS analysis of amorphized area

The EXELFS analysis was conducted on the completely amorphized area and the resultant PRDFs around Si and C atoms are shown in Figs. 13(a) and 13(b), respectively. The data ranges in the wave number used for the Fourier transformation were 33.5–129.5 nm⁻¹ (42.8–639.0 eV above the spectrum onset) and 27.5–80 nm⁻¹ (28.8–243.9 eV) for the Si and C *K* edges, respectively. The data range available for carbon was limited because a significant amount of oxygen was included, probably owing to surface oxide, whose absorption edge started from ~530 eV. Hence the peak separation (resolution) of the C PRDF is much worse than that in the Si PRDF. Note that the peak positions in the PRDFs are shifted from the true interatomic distances to the shorter side because no correction for the phase shift was made.²⁶

Each peak in the PRDF should correspond to an amplitude-modulated sine wave in the *k* space, whose frequency and phase are determined by the interatomic distance and the electron scattering power of the corresponding atom pair.^{26,29,30} In the present case one has to take into account Si-Si and Si-C pairs for the Si PRDF and C-C and C-Si pairs for the C PRDF. The peaks up to $r=0.4$ nm were assigned to the specific atom pairs in the following manner: in tetrahedrally coordinated semiconductors and ceramics, the most probable structural unit even in amorphous structure is the most stable triangle with the two sides of the stable covalent bonds making an angle of 109.5°. The possible unit triangles to be considered in the present case are shown in Fig. 13(c). Each atom pair in the figure gives a peak position and a phase shift in the PRDFs, which can be determined by an *ab initio* calculation.³⁴ Each peak in the PRDFs was thus

assigned to the specific atom pair illustrated in (c) consistently, as indicated in Figs. 13(a) and 13(b). It should be noted that the first peak in (b) was assigned to Si–C(1) and C–C(1) pairs overlapping, considering the intrinsic peak width and asymmetry. The observed C–C(1) pair should be of sp^3 type because the second peak position assigned to C–C(2) in (b) is also consistent with the sp^3 bond length.

4. ELNES of amorphized area

The fine structures of C *K* and Si *L* absorption edges (ELNES) from the unirradiated and amorphized areas are shown in Figs. 14(a) and 14(b), respectively. The fine structures were lost by the irradiation, which is more conspicuously seen in the C *K* ELNES. This simply reflects the loss of the long-range order and chemical disordering.

We carefully examined the C *K* ELNES from the amorphized area to see if the sp^2 type C–C bonding occurred by the irradiation, when the additional π^* peak appear at the lower energy side of the edge. A very small amount of π – π^* transition at the irradiated areas was sometimes found but soon vanished during the EELS measurement. This indicates that the π^* peaks originated from the surface graphitized layers formed by the irradiation and the layers were evaporated by the illumination of intense electrons for the EELS measurement. This suggests that the C–C bonds formed by the irradiation are of sp^3 type except the surface regions, consistent with the previous EXELFS results.

IV. DISCUSSION

A. Damage processes of SiC below and above T_c

Key observations to discuss the damage processes of electron-irradiated SiC are: (i) the critical dose necessary for complete amorphization was nearly independent of irradiation temperature well below T_c . (ii) The plasmon shift during the irradiation was independent of sample thickness below T_c , while it was strongly dependent on the sample thickness above T_c . (iii) Above T_c , the crystal structure of the irradiated area was fragmented into nanometer size crystallites, slightly misoriented relative to the original crystal orientation. (iv) Above T_c , the carbon content was more depleted than that of silicon at the irradiated area, leaving silicon nanoclusters. In contrast, the composition of the amorphized area remained unchanged below T_c . (v) Below T_c , the amorphized structure consisted of rather homogeneous mixture of Si–C, Si–Si, and C–C covalent bonds, most of which kept the stable tetrahedral configuration. (vi) No stable sp^2 C–C bonds were found except for the surface regions in the irradiated areas both above and below T_c . Meanwhile, it is known that there is a minor step in the critical dose to amorphized SiC that occurs near 90 K,^{4,5} though we do not discuss this issue here because all the experiments of the present study were conducted above this temperature range.

The above observations suggest that the main controlling factor of the damage process is the mobility of displaced atoms. A recent MD simulation³⁹ has suggested that a carbon and silicon interstitial is mobile above RT and 350 K, respectively, in a SiC crystal. Below T_c , atoms displaced to inter-

stitial positions by electron irradiation will reconstruct the surrounding atoms and be frozen at the relaxed positions, the phenomenon of which should be thickness independent. Subsequent displacements and structural relaxation will give rise to amorphized regions extending over a few atomic distances.

Above T_c , on the other hand, thermal recovery by mobile interstitial atoms plays an essential role: lighter carbon atoms should be preferentially displaced and diffuse away out of the irradiated area, probably toward the surface sink for a thinner sample. Resulting excess silicon atoms, that are much less mobile, would reconstruct the broken bonds to lessen the number of unsaturated bonds. This tendency will be enhanced by the fact that it is more energetically favorable for Si to occupy a vacant C site than for C to occupy a Si site.⁴⁰ The resultant lattice distortions associated with the local Si clustering give rise to the local lattice bending, though the overall crystal structure is well maintained because the “flexible” Si sublattice bears the majority of the lattice relaxation.

Weber⁴¹ classified amorphization of materials due to irradiation into several mechanisms by the damage evolution versus irradiation dose: (1) direct-impact (in cascade) within an individual collision cascade; (2) the local accumulation of high defect concentrations due to the overlap of collision cascades; (3) the nucleation and growth process; and (4) a combination of these processes, such as direct impact combined with cascade overlap or direct impact combined with stimulated amorphization at C/A interfaces. The evolution of amorphous fraction as a function of irradiation dose, D , follows $1 - \exp(-\sigma D)$ for the mechanism (1), while the other mechanisms exhibit sigmoidal-like dependence of relative disorder on dose. If the plasmon shift associated with amorphization corresponds to the evolution of the amorphous fraction, as mentioned in Sec. III B 1, a process similar to the direct-impact model seems to explain the present exponential decay of E_p in Fig. 11. In the case of the present electron irradiation, it would be more appropriate to adopt “defect accumulation model” to predict the linear accumulation of amorphous volume.^{18,42} The kinetics of amorphization well below T_c could be hence expressed by the following equation:⁴³

$$\frac{df_a}{dt} = \phi\sigma(1 - f_a), \quad (6)$$

where ϕ is the electron flux, σ is the cross section for direct displacement, and the term $(1 - f_a)$ accounts for the crystalline fraction available for amorphization. Equation (6) does not include the thermal recovery term, reflecting the key observation (i) above.

The solution of Eq. (6) under the initial condition $f_a(t=0)=0$ is

$$f_a = 1 - \exp(-\phi\sigma t). \quad (7)$$

When the plasmon energies for crystalline and amorphous portions are assigned to E_p^c and E_p^a , respectively, the observed plasmon peak is located at $f_a E_p^a + (1 - f_a) E_p^c$, assuming that the plasmon peak position is given by the weighted average of the plasmon energies involved. The last assump-

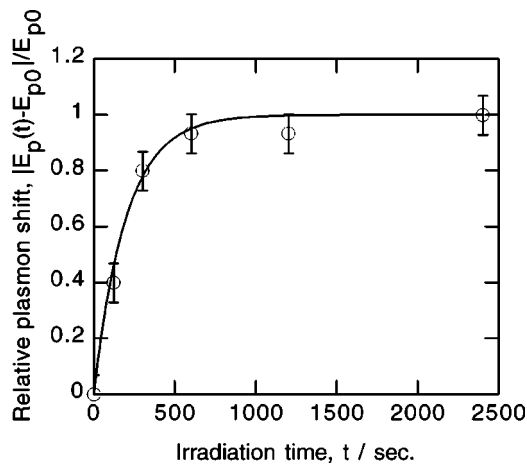


FIG. 15. Replot of Fig. 10 (open circles) as a function of irradiation time and their fit by Eq. (8) (solid curve).

tion is justified when $|E_p^c - E_p^a|/E_p^c \ll 1$. The plasmon shift as a function of irradiation time $\Delta E_p(t)$ is then expressed by

$$\Delta E_p = E_p(t) - E_p^c = (E_p^a - E_p^c)(1 - \exp[-\phi\sigma t]). \quad (8)$$

The cross section of displacement damage can be thus estimated by fitting the relative plasmon shift with Eq. (8), as shown in Fig. 15. E_p^c and E_p^a are the plasmon energies before the irradiation and after the full amorphization, respectively. σ was estimated to be $(2.8 \pm 0.5) \times 10^{-24} \text{ cm}^{-2}$, while the displacement cross section calculated by the known McKinley-Feshbach formula for electron scattering [Eq. (1)] was $\sim 2.8 \times 10^{-25} \text{ cm}^{-2}$ for Si and $\sim 1.4 \times 10^{-24} \text{ cm}^{-2}$ for C. Each displaced atom is therefore supposed to contribute to the local structural disordering over a few to about ten atoms surrounding it. This small cascade size for each displacement effectively rules out the stimulated damage evolution at the C/A interface, unlike the cases for heavy ion or high-energy neutron irradiation. Furthermore, if correlated point defect recombination to produce recovery of the created Frenkel defects is taken into account, the size of local disordering should be accordingly larger by double or more.

The present analysis is justified only if the envelope of the wave function of the plasmon is localized within the small cascade for each displacement. A plasmon actually extends over only a few lattice sites for a large class of metals and semiconductors.⁴⁴ In addition the threshold displacement energies used in the present analysis were taken as 70 and 40 eV for Si and C, respectively, which might be larger than the lowest ones (35 and 20 eV) reported in other articles.⁴⁵⁻⁴⁷ Even if we take these lowest values as the threshold energies, the above discussion holds just by changing the dpa estimation to about a half of them and the cross section of displacement damage calculated by McKinley-Feshbach formula accordingly.

B. Origin of large volume swelling associated with amorphization

The key observations (v) and (vi) described in Sec. IV A suggest that the homonuclear bonds can bear a part of the volume swelling, because the simple arithmetic average of

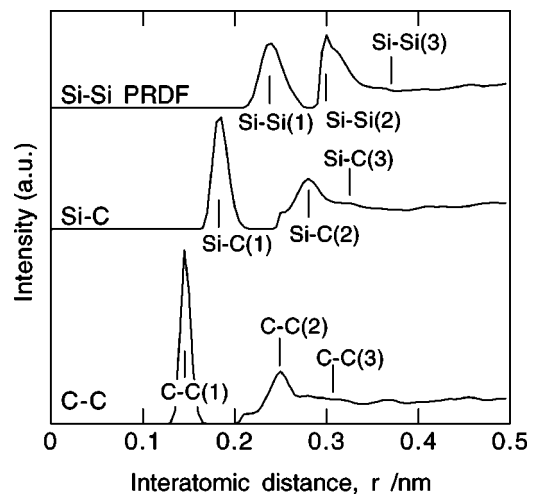


FIG. 16. PRDFs of amorphous SiC generated with MD by melt and quench method.

covalent bond lengths of Si-Si, Si-C, and C-C gives 0.193 nm for $r_{\text{C-C}} = 0.154 \text{ nm}$ (sp^3), but 0.189 nm for $r_{\text{C-C}} = 0.142 \text{ nm}$ (sp^2) that is equal to the original Si-C bond length. The increase in the average bond length should cause a certain volume expansion. In order to see how much volume increase is expected by this increase in the average bond length, an amorphous structure was generated using MD.

A cubic MD cell containing 1000 atoms (500 Si and 500 C) randomly arranged was prepared. The system was first retained at 4000 K for 20 ps (20 000 steps) under the NTP ensemble (constant number of particles, temperature and pressure), when the system was completely melted. The interatomic potential used was the Tersoff potential for SiC,⁴⁸ which does not take the sp^2 type C-C interaction into account. The system was then cooled down to 300 K at the cooling rate of 50 K/ps and amorphous SiC structure was thus obtained. The corresponding PRDFs are shown in Fig. 16. The primary peak positions up to $\sim 0.3 \text{ nm}$ are in good agreement with those obtained by EXELFS analysis, as shown in Fig. 13. The atomic density was decreased (or the volume was increased) by 7%. Therefore one half of the observed swelling is explained by the increase in the average bond length due to formation of sp^3 C-C bonds.

The other half of the observed swelling is likely ascribed to introduction of Frenkel pairs. Another MD simulation was then carried out to estimate how much volume is increased by introduction of a pair of interstitial and vacancy. A Si or C atom was removed from the cubic MD cell [$5 \times 5 \times 5$ unit cells (1000 atoms), zincblende structure] and inserted back into an appropriate interstitial position. The MD was run at 300 K for 10 ps to let the surrounding atomic positions relax. As a result, the volume was increased by $5.2 \times 10^{-2}\%$ and $4.4 \times 10^{-2}\%$ per Si-V (vacancy) and C-V pair for 1000 atoms, respectively, nearly independent of the initial interstitial position. Since at least 1/10 of atoms (or 100 atoms in this case) are to be displaced for complete amorphization according to the discussion in Sec. IV A, the expected void swelling can be estimated to be more than 4%–5%. Hence the total observed volume swelling can be fully explained by the increase in the average bond length due to the formation

of sp^3 C–C and the conventional void swelling. Recently Snead and Zinkle showed that volumetric swelling of amorphous SiC could vary a wide range ($\sim 5\%$) prior to recrystallization by annealing.⁴⁹ They attributed it to annealing out local strain in the amorphous network. This can be explained by the sp^3 C–C bonds changing to more stable sp^2 bonds during annealing.

V. CONCLUSIONS

Damage processes of α -SiC above and below the critical temperature (T_c) of amorphization by high-energy electron irradiation were examined by means of TEM and EELS.

Amorphization occurring below T_c proceeds by subsequent formation and accumulation of small disordered regions extending over a few lattice sites, each of which is formed by reconstruction of unsaturated bonds and strain relaxation around the displaced atom. The kinetics of amorphization is well explained by the defect-accumulation model. The amorphous structure can be characterized by a homogeneous mixture of Si–Si, Si–C, and C–C covalent bonds, excluding sp^2 -type C–C bond formation except for surface regions, and the building blocks of the structure still tend to keep the tetrahedral coordination. Furthermore, the large volume swelling associated with the amorphization is ascribed to the increase in the average bond length in addition to the conventional void swelling.

On the other hand, the crystal structure is retained by the irradiation above T_c , although the crystal is fragmented into a highly defective state in which the crystal lattices are locally misoriented to one another. This structure is formed by local strain centers induced by preferential displacements and outward diffusion of lighter C atoms, followed by clustering of excess Si atoms. The mechanisms of the damage processes are totally controlled by the mobility of self-interstitial atoms and the tendency of covalent bonding to minimize the number of unsaturated bonds. Hence the present mechanisms would hold true universally for damaging processes of any covalent bonded materials.

ACKNOWLEDGMENTS

The authors are grateful to Professor H. Takahashi, Dr. T. Shibayama, and K. Sugawara of CARET, Hokkaido University, and Messrs. S. Arai and C. Morita of CIRSE, Nagoya University for their technical support in operating the ultra high-voltage TEMs. They also thank Dr. T. Maruyama of The Wakasawan Energy Research Center for kindly letting us use the energy-filtering TEM. One of the authors (S.M.) would like to express cordial thanks to Professor G. Van Tendeloo and Dr. Y. Verbeeck of EMAT, University of Antwerp for their support in obtaining a part of EXELFS spectra. This work is partly supported by Grant-in-Aid for Scientific Research by Ministry of Education, Culture, Sports, Science and Technology in Japan.

¹E. Wendler, A. Heft, and W. Wesch, Nucl. Instrum. Methods Phys. Res. B **141**, 105 (1998).

²W. J. Weber, N. Yu, L. M. Wang, and N. J. Hess, Mater. Sci. Eng., A **253**, 62 (1998).

- ³P. Fenici, A. J. F. Rebels, R. H. Jones, A. Kohyama, and L. L. Snead, J. Nucl. Mater. **258**, 215 (1998).
- ⁴H. Inui, H. Mori, and H. Fujita, Philos. Mag. B **61**, 107 (1990).
- ⁵H. Inui, H. Mori, A. Suzuki, and H. Fujita, Philos. Mag. B **65**, 1 (1992).
- ⁶A. Matsunaga, C. Kinoshita, K. Nakai, and Y. Tomokiyo, J. Nucl. Mater. **179–181**, 457 (1991).
- ⁷L. L. Snead, S. J. Zinkle, J. C. Hay, and M. C. Osborne, Nucl. Instrum. Methods Phys. Res. B **141**, 123 (1998).
- ⁸L. L. Snead and J. C. Hay, J. Nucl. Mater. **273**, 213 (1999).
- ⁹D. P. White, J. Appl. Phys. **73**, 2254 (1993).
- ¹⁰R. R. Hart, H. J. Dunlap, and O. J. Marsh, Radiat. Eff. **9**, 261 (1971).
- ¹¹J. M. Williams, C. J. McHargue, and B. R. Appleton, Nucl. Instrum. Methods **209/210**, 317 (1983).
- ¹²J. A. Spiznagel *et al.*, Nucl. Instrum. Methods Phys. Res. B **16**, 237 (1986).
- ¹³J. A. Edmond, R. F. Davis, S. P. Withrow, and K. L. Move, J. Mater. Res. **3**, 321 (1998).
- ¹⁴N. G. Chechenin *et al.*, Nucl. Instrum. Methods Phys. Res. B **65**, 341 (1992).
- ¹⁵L. L. Horton *et al.*, Nucl. Instrum. Methods Phys. Res. B **65**, 345 (1992).
- ¹⁶L. W. Hobbs, A. N. Sreeram, C. E. Jesurum, and B. A. Berger, Nucl. Instrum. Methods Phys. Res. B **116**, 18 (1996).
- ¹⁷P. K. Gupta and A. R. Cooper, J. Non-Cryst. Solids **123**, 14 (1990).
- ¹⁸W. Bolse, Nucl. Instrum. Methods Phys. Res. B **141**, 133 (1998).
- ¹⁹S. Grigull, M. Ishimaru, M. Nastasi, C. A. Zorman, and M. Mehregany, Philos. Mag. Lett. **81**, 55 (2001).
- ²⁰F. Gao and W. J. Weber, Phys. Rev. B **63**, 054101 (2000).
- ²¹F. Gao and W. J. Weber, J. Appl. Phys. **89**, 4275 (2001).
- ²²F. Gao, W. J. Weber, and W. Jiang, Phys. Rev. B **63**, 214106 (2001).
- ²³J. M. Perlado, L. Malerba, and T. Diaz de la Rubia, Mater. Res. Soc. Symp. Proc. **540**, 171 (1999).
- ²⁴W. A. McKinley and H. Feshbach, Phys. Rev. **74**, 1759 (1948).
- ²⁵P. B. Hirsch, A. Howie, R. B. Nicholson, D. W. Pashley, and M. J. Whelan, *Electron Microscopy of Thin Crystals* (Krieger, Malabar, 1977), Chap. 14.
- ²⁶R. F. Egerton, *Electron Energy-Loss Spectroscopy in the Electron Microscope* (Plenum, New York, 1996).
- ²⁷H. Chang and A. J. Bard, J. Am. Chem. Soc. **113**, 5588 (1991).
- ²⁸S. Igarashi, S. Muto, T. Tanabe, and T. Maruyama, Mater. Trans., JIM **42**, 2131 (2001).
- ²⁹L. Reimer, in *Energy-Filtering Transmission Electron Microscopy* (Springer, Berlin, 1995), Chap. 7.2.1.
- ³⁰N. Asaoka, S. Muto, and T. Tanabe, Diamond Relat. Mater. **10**, 1251 (2001).
- ³¹R. L. McGreevy and L. Pusztai, Mol. Simul. **1**, 359 (1989).
- ³²S. J. Gurman and R. L. McGreevy, J. Phys.: Condens. Matter **2**, 9463 (1990).
- ³³S. Muto and T. Tanabe, J. Electron Microsc. (to be published).
- ³⁴A. L. Ankudinov, B. Ravel, J. J. Rehr, and S. D. Conradson, Phys. Rev. B **58**, 7565 (1998).
- ³⁵A. Le Bail, <http://pcb4122.univ-lemans.fr/glasses/glassvir.html>
- ³⁶<http://www.cristal.org/vrml/intvrml.html>
- ³⁷J. M. Cowley, *Diffraction Physics*, 3rd rev. ed. (Elsevier, New York, 1995), Chap. 11.
- ³⁸A. Filippini, E. Bernieri, and S. Mobilio, Phys. Rev. B **38**, 3298 (1998).
- ³⁹H. C. Huang, N. M. Goniem, J. K. Wong, and M. I. Baskes, Modell. Simul. Mater. Sci. Eng. **3**, 615 (1995).
- ⁴⁰S. Muto, T. Tanabe, T. Shibayama, and H. Takahashi, Nucl. Instrum. Methods Phys. Res. B **191**, 519 (2002).
- ⁴¹W. J. Weber, Nucl. Instrum. Methods Phys. Res. B **166–167**, 98 (2000).
- ⁴²W. Bolse, J. Conrad, T. Rodle, and T. Weber, Nucl. Instrum. Methods Phys. Res. B **118**, 748 (1996).
- ⁴³W. J. Weber and L. M. Wang, Nucl. Instrum. Methods Phys. Res. B **91**, 63 (1994).
- ⁴⁴J. Roganand and J. E. Inglesfield, J. Phys. C **14**, 3585 (1981).
- ⁴⁵S. J. Zinkle and C. Kinoshita, J. Nucl. Mater. **251**, 200 (1997).
- ⁴⁶W. Windl, T. J. Lenosky, J. D. Kress, and A. F. Voter, Nucl. Instrum. Methods Phys. Res. B **142**, 61 (1998).
- ⁴⁷R. Devanathan, W. J. Weber, and F. Gao, J. Appl. Phys. **90**, 2303 (2001).
- ⁴⁸J. Tersoff, Phys. Rev. B **49**, 16349 (1994).
- ⁴⁹L. L. Snead and S. J. Zinkle, Nucl. Instrum. Methods Phys. Res. B **191**, 497 (2002).